Remote sensing of suspended sediment concentration during turbid flood conditions on the Feather River, California— A modeling approach

Nina E. Kilham,[1,2] Dar Roberts,[1] and Michael B. Singer[3,4]

[1] Direct measurements of suspended sediment concentration (SSC) in rivers are surprisingly sparse. We present an approach for measuring these concentrations from space, tailored to fit rivers with limited records of flood-level SSC. Our approach requires knowledge of a typical particle-size distribution of sediment suspended during floods, the dominant mineralogy, and a calibration consisting of above-water reflectance field spectra with known SSC. Surface SSC values were derived for two Landsat images covering 70 km of the Feather and portions of the Sacramento, Yuba, and Bear Rivers in California in order to capture conditions during a large flood event. Using optical theory and radiative transfer modeling we modeled remote-sensing reflectance (R_{rs}) for a number of three-component mixtures composed of color dissolved organic matter (CDOM), water, and montmorillonite particles. We then iteratively estimated CDOM by fitting modeled spectra for a range of absorption coefficients to field-measured spectra collected from the Sacramento River and matched to measured SSC values. Spectral mixture analysis with a two-end-member model yielded end-member fractions and SSC via a look-up table specific to the Landsat sensor. Model closure was within the error of measured SSC values, suggesting that this approach is promising for deriving SSC on rivers during flood conditions when empirical relationships established between low SSC values and R_{rs} are no longer valid.

1. Introduction

[2] Since the 1970s, remotely acquired optical imagery has been used to quantify surface sediment concentrations in sufficiently large water bodies [see reviews by *Mertes et al.*, 2004; *Ritchie et al.*, 2003a]. Such methods show promise for obtaining sediment concentrations and fluxes in rivers lacking direct measurements of suspended load, potentially providing valuable information on the role of floods in transporting sediment. With the present suite of satellites carrying optical instruments, image analysis could be used to regularly monitor suspended sediment transport conditions during large floods when high sediment concentrations and hazardous conditions otherwise inhibit sampling. Furthermore, imagery provides a synoptic assessment of the river system—a unique benefit that allows for both the setting of initial conditions and/or validation of suspended sediment transport predicted by multidimensional numerical models [*Dekker et al.*, 2001; *Ouillon et al.*, 2004].

[3] Regularly quantifying suspended sediment concentrations in large rivers with consistent methods would highlight seasonal and interannual variations, and mapping the spatial distribution of sediment loading could provide information on sediment sources. Both temporal and spatial trends are relevant for understanding large-scale biogeochemical cycling—especially of carbon as river discharge provides the primary pathway for carbon burial in oceans, contributing an estimated 6×10^{12} kg of sediment to the world's oceans each year [*Milliman and Meade*, 1983]. Furthermore, suspended sediment delivery to floodplains counteracts lateral erosion due to channel migration, contributing to floodplain maintenance and intrabasin storage of associated nutrients and contaminants.

[4] Although remote sensing is used widely to monitor oceans and lakes, its application to river systems is hampered by two crucial difficulties. First, image-derived measurements represent the concentration of suspended sediment within a surface layer—thus necessitating conversion to a depth-integrated load before comparison to numerical models or field measurements. Second, most methods have relied upon empirical relationships between sediment concentrations and the water-leaving reflectance captured by the remote sensing instrument [*Ritchie et al.*, 2003a; *Ruhl et al.*, 2001; *Whitlock et al.*, 1981]. Empirical calibrations using remotely sensed or field-derived reflectance data

[1]Department of Geography, University of California, Santa Barbara, California, USA.
[2]Delta Modeling Associates, San Francisco, California, USA.
[3]School of Geography and Geosciences, University of St. Andrews, St. Andrews, UK.
[4]Earth Research Institute, University of California, Santa Barbara, California, USA.

provide site-specific predictions of water quality parameters with reasonable accuracy [e.g., *Ritchie et al.*, 2003b; *Ruhl et al.*, 2001; *Whitlock et al.*, 1981], but are limited in their universal application and may not extend to the full range of conditions present in inland waters [*Schiebe et al.*, 1992]. Although several workers have identified a linear relationship between suspended sediment concentration (SSC) and reflectance within a concentration range of 0 to 50 mg L^{-1} [*Munday and Alfoldi*, 1979; *Ritchie et al.*, 2003b], an exponential relationship clearly exists at higher concentrations [*Curran and Novo*, 1988; *Holyer*, 1978; *Schiebe et al.*, 1992]. Thus calibrations established during lower flows do not apply to more turbid conditions because of the nonlinear response of reflectance to increasing sediment levels [*Jonasz and Fournier*, 2007; *Pavelsky and Smith*, 2009; *Ritchie et al.*, 2003a; *Schiebe et al.*, 1992; *Witte*, 1982]. Consequently, establishing a physical basis for modeling the water-leaving reflectance for a given concentration could prove to more reliably assess SSC. Furthermore, this would present a general approach which could be applied across a range of rivers, a range of conditions, and over several decades of imagery.

[5] In this paper we seek to establish a framework for a universal approach for deriving SSC in rivers from remote sensing imagery. We emphasize that our primary contribution is to synthesize the work of others into a unifying framework, fundamentally based on physical theory, and specific to turbid rivers. Because we hope that this framework will be tested by others, we purposely designed this study to rely upon the minimum amount of easily obtainable in situ data and model code. More specifically, we:

[6] 1. Present model coefficients describing the inherent optical properties of a specific type (color, density) and size distribution of inorganic and organic particles suspended in water.

[7] 2. Generate end members (sets of water-leaving reflectance spectra) for each of several combinations of SSC and other relevant water constituents impacting the remote-sensing signal.

[8] 3. Invert the end members with field measurements of the water-leaving spectral reflectance for a given SSC to obtain reasonable values of the other water constituents.

[9] 4. Decompose the signal in two Landsat images using a spectral mixture analysis approach with the site-specific model end members to arrive at surface values of SSC in mg L^{-1}.

[10] A theoretical approach, which accounts for the dependency of the form and magnitude of the water-leaving spectra on sediment mineralogy and particle-size distribution, appears promising for meeting our objective of a physically based, universally applicable approach to inferring high SSC in rivers.

2. Theoretical Background

2.1. Toward a Universal Sediment Concentration Model for Remote Sensing

[11] *Holyer* [1978] addressed development of universal sediment concentration algorithms and found that sufficient conditions for universality existed if the particle-size distribution of the sediment source can be accounted for. Other water optical properties have been found to transfer across

a range of suspended sediment particle sizes, including nephelometric turbidity units [*Holyer*, 1978], beam attenuation [*Gould and Arnone*, 1997], and diffuse light attenuation [*Woodruff et al.*, 1999]. However, a relationship between these parameters and SSC is then necessary, which is subject to the same particle-size considerations.

[12] A more theoretical approach follows models developed by oceanographers, which simulate the volume reflectance of the water column based upon quantitative knowledge of the optical properties of the water and sediment. Optical modeling is preferable to the (semi-) empirical algorithms described above, as these models are able to account for the range of water conditions present in turbid (case 2) and extremely turbid (case 3) water bodies [*Stumpf and Pennock*, 1989]. These models range from generic radiative transfer models (e.g., hydrolight [*Mobley*, 1994]) to models which only address the suspended sediment component of the water through semianalytical solutions [e.g., *Albanakis*, 1990; *Woodruff et al.*, 1999].

[13] Recent approaches mainly use parameterized bio-optical models that are subsequently inverted [*Dekker et al.*, 2001; *Hoogenboom et al.*, 1998]. Inversion of the radiative transfer model can be achieved through methods such as iterative fitting with a minimization scheme, or artificial neural networks [*Durand et al.*, 2000]. Both methods require that the domain of variability of the input parameters—e.g., chlorophyll levels, SSC, colored dissolved organic matter absorption—is known a priori. Iterative fitting approaches used by *Frette et al.* [1998], for example, rely on χ^2 values between the modeled and measured spectral radiances. This can become computationally expensive when several spectral bands are used, however the use of hyperspectral data mitigates the problem of multiple solutions (i.e., multiple combinations of the model variable may combine to give the same reflectance spectra). Neural networks can automate this process, although they also require extensive a posteriori analysis [*Durand et al.*, 2000].

2.2. Governing Theory Behind Optical and Radiative Transfer Modeling

[14] The following discussion is intended to provide the reader with a basic understanding of the processes by which light interacts with water, water constituents, and the atmosphere. We have drawn heavily upon work by *Mobley* [1994], *Kirk* [1994], *Bricaud and Morel* [1986], and *Wozniak and Stramski* [2004], and refer the interested reader to these publications for further details.

[15] We begin by following the path of light collected by a hand-held field radiometer. When placed just above the surface of a water body, the radiometer captures upward directed light that is a product of the scattering of incident sunlight and skylight by suspended particles and water molecules, and absorption of the light by water and dissolved substances [*Kirk*, 1994]. Together these two processes describe the total attenuation of light by a specific layer of the water body:

$$c = a + b, \qquad (1)$$

where a, b, and c are the absorption, scattering, and the beam attenuation coefficients (m^{-1}), respectively. Since they are independent of the geometric structure of the light

field, and only depend upon the substances dissolved or suspended in the water, these coefficients are *inherent optical properties* (IOP) [*Kirk*, 1994]. The total amount of light attenuation by the layer of the water body can then be expressed as a sum of the absorption $a_i(\lambda)$, scattering $b_i(\lambda)$, or backscattering coefficients $b_{Bi}(\lambda)$ attributed to each optically active component, indexed by i, of a mixture, with the amount dependent on the *optical cross section* available for photon interaction. Since mineral particles dominate the emergent spectra in case 2 (turbid) water bodies, simulating the volume reflectance measured by a field radiometer involves determining the concentration, particle-size distribution, and optical properties of these particles.

[16] Optical cross sections can be theoretically derived by solving the set of equations governing electromagnetic behavior for the case of a plane wave of light illuminating a sphere. Generally attributed to *Mie* [1908], these equations offer an exact solution to the Maxwell equations for isotropic, homogeneous spheres in a sufficiently dilute suspension so that scattering is incoherent. Solving these equations yields dimensionless efficiency factors expressing the amount of incident light absorbed, scattered, or backscattered by the suspended minerals. These factors are then normalized by the geometrical cross-sectional areas of the particles to give their respective optical cross sections. Once the optical properties are determined, a relationship can be derived between these properties and the incident light field in order to describe how radiance varies with distance along any specified path into, or exiting the water.

[17] At the top of the atmosphere, the total radiance measured by a remote sensing instrument over a water body can be conceptualized as the sum of four components (modified from *Legleiter et al.* [2004]):

$$L_t(\lambda) = L_B(\lambda) + L_w(\lambda) + L_s(\lambda) + L_{\text{path}}(\lambda), \qquad (2)$$

where $L_t(\lambda)$ (W m^{-2} sr^{-1} nm^{-1}) is the radiance at the top of the atmosphere, $L_B(\lambda)$ is the radiance that has transmitted through the water column, reflected off the channel substrate, and transmitted through the atmosphere before reaching the sensor, $L_w(\lambda)$ is the water-leaving radiance due to the water column alone, $L_s(\lambda)$ is the radiance of sunlight reflected directly off the water surface without interacting with the water column, and $L_{\text{path}}(\lambda)$ refers to the *path radiance*—e.g., scattering due to air molecules and aerosol particles (dust, water droplets, salt, etc.) within the atmosphere. If the data are screened for sun glint, and for sufficiently deep and turbid water bodies where light is scattered upward before reaching the bottom, $L_w(\lambda)$ can be solved for by

$$L_w(\lambda) = \frac{L_t(\lambda) - L_{\text{path}}(\lambda)}{\tau}, \qquad (3)$$

where τ is the atmospheric transmittance.

[18] Measuring the water-leaving radiance L_w directly above the water surface is not possible since the signal collected by the radiometer includes both L_w and skylight (L_s) reflected off the water surface into the direction of the sensor (L_r). Thus L_w must be determined indirectly in the field by subtracting the reflected skylight component from the total signal (L_t). In practice, the relationship between L_s

and L_r is estimated using a proportionality factor (ρ), which depends upon the direction, wavelength, wave-surface slope, detector field-of-view (FOV), and on the incident sky radiance distribution. With a uniform sky radiance distribution, and a level water surface, this factor represents the average of the Fresnel reflectance over the detector FOV [*Mobley*, 1999].

[19] Finally, if the radiometer measurements are taken above the water surface, we also need to account for transmittance across the air/water boundary. Using the relationship proposed by *Mobley* [1994], the emergent flux at the water surface is

$$L_w(\theta', \phi, \lambda) = \frac{t \cdot L_u(\theta, \phi, z = 0, \lambda)}{n_w^2} \qquad (4)$$

showing that L_w (W m^{-2} sr^{-1} nm^{-1}) at a specific zenith θ', azimuthal angle ϕ, and wavelength λ is related to the upward-flux beneath the water surface $L_u(\theta, \phi\ z = 0, \lambda)$ by a factor (t/n_w^2) which accounts for losses due to internal reflection and refraction at the water/air boundary. For a flat water surface, *Austin* [1980] proposed a transmittance (t) of 0.979 across the interface, which along with the refractive index for water at 20°C ($n_w = 1.333$) gives a value of 0.551 for this factor.

[20] Relating the radiance values measured just above the water surface to those acquired by a remote sensing instrument then involves converting this radiance value to units of reflectance specific to remote sensing, defined as

$$R_{rs}(\theta', \phi, \lambda) = \frac{L_w(\theta', \phi, \lambda)}{E_d(\lambda)}, \qquad (5)$$

where $E_d(\lambda)$ is the downwelling spectral irradiance (W m^{-2} nm^{-1}) of sunlight incident upon the water surface.

[21] Equation (5) can be approximated at each wavelength by

$$R_{rs} = \frac{(L_t - \rho L_s)}{\left(\dfrac{\pi}{R_g} L_g\right)}, \qquad (6)$$

where the denominator is E_d as it is commonly measured in the field, by measuring the radiance (L_g) of a gray surface (usually a plaque made of Spectralon) with a known irradiance reflectance R_g, which is a Lambertian (isotropic) reflector to a good approximation.

2.3. Spectral Mixture Analysis

[22] SMA determines the contribution by several components to a signal. It relies on set end members of known, pure components, independent of the image being analyzed. Each image pixel encodes information on the reflectance properties of a mixture of materials present within the projected ground area. Where the entire pixel is a water mixture, a linear end-member model can be used to determine the relative contributions by each "pure" component to the reflectance spectra for that pixel, via

$$r(x, y) = \alpha M + \varepsilon, \qquad (7)$$

where $r(x,y)$ is the reflectance spectrum for the pixel at position (x,y); α is the vector of end-member abundances;

M is the matrix of end-member spectra, and ε is the vector of residuals between the modeled and measured reflectance. The result of the mixture analysis is a series of "fraction images" in which the data values represent the fraction contribution by each end member. For our purposes, an "end member" constitutes water with optically active constituents present at varying levels of concentration.

3. Methods

3.1. Overview

[23] We outline our methodological strategy in Figure 1. In practice we first obtained simultaneous samples of surface SSC (mg L^{-1}), $L_t(\lambda)$, and $E_d(\lambda)$ by boat on the Feather River in Northern California (Figure 2). Using these measurements and equation (6) we generated spectra for each sediment concentration (Figure 1). We then solved optical equations for sediment specific to that carried in suspension by the Feather River. Using mass-specific absorption and scattering coefficients for the suspended sediment, and for pure water, and the atmospheric conditions during the field campaign, we solved the radiative transfer equations to derive $R_{rs}(\theta', \varphi, \lambda)$ for several combinations of SSC and the absorption by color dissolved organic matter. Because we did not know the levels of other optically active constituents in the river water at the time, we inferred these levels by inverting several modeled spectra with the field measurements to select the "best-fit" end members for a given level of color dissolved organic matter absorption. Linear mixture analysis was then used twice. First we applied this

to the modeled end members in order to construct a calibration curve relating end-member fractions to SSC. This provided us with a set of end members which could then be used to derive sediment concentrations from any remotely derived image. We then applied this end-member set to two Landsat images acquired during past floods on the Feather River. After correcting for atmospheric interference and converting to reflectance units, linear mixture analysis was applied to both images using two end members to bracket the expected range of SSC during each flood. The resulting fraction values were then converted to SSC in mg L^{-1} using the calibration curve specific to Landsat.

3.2. Field Measurements

[24] The Feather River (Figure 2) drains the western Sierra Nevada Mountains and is enclosed by levees extending about 70 km from impoundment at Oroville Dam to the confluence with the Sacramento River. In February 2006 we measured $R_{rs}(\theta', \varphi, \lambda)$ and SSC at several locations along the Sacramento and Feather Rivers (Figure 3). Satellite stage heights were 13 m on the Sacramento (Wilkins Slough, USGS 11390500) on 15 February and 10 m on the Feather (near Boyd's, USGS 390328121363901) on 16 February at noon. Suspended sediment was measured using a Van Dorn sampler suspended off a boat just below the water surface to capture the volume penetrated by the sensor ($\sim$0.25 m, see section 3.3.1). At two locations (SR1 and SR4) we also collected a second, deeper sample at $\sim$2 m. Total suspended sediment was then measured in the laboratory using standard vacuum filtration methods (ASTM D3977–97), and a
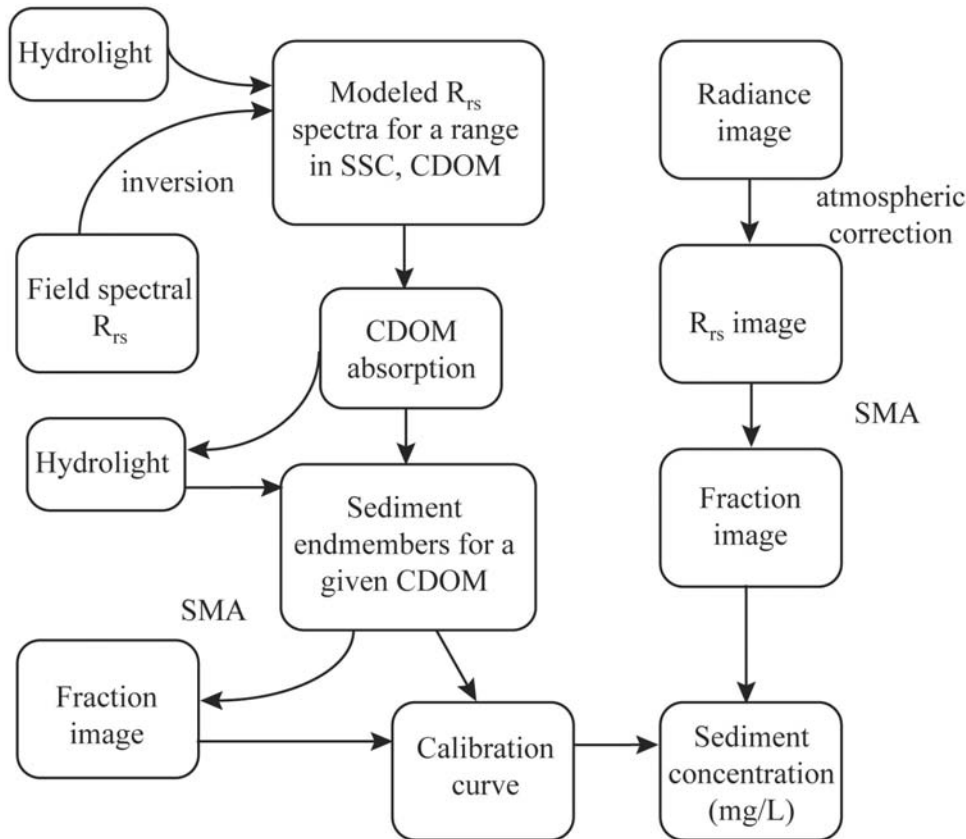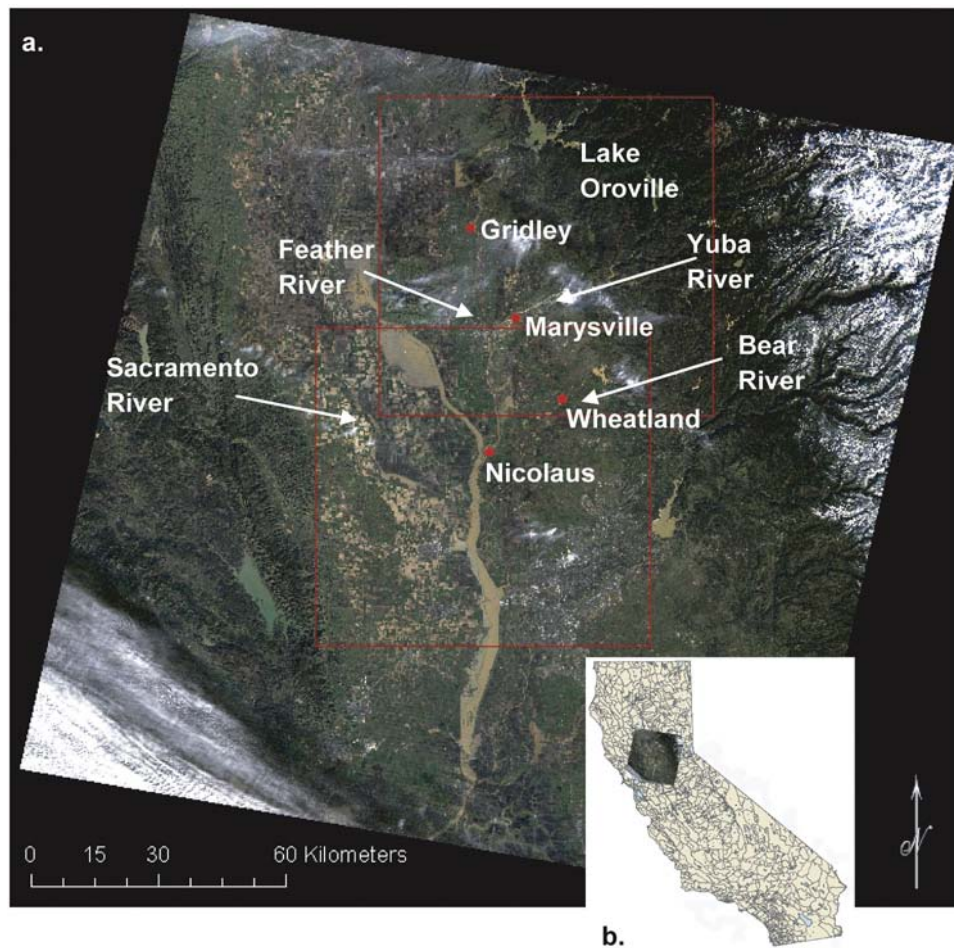

Figure 1. General modeling approach.

Figure 2. (a) True-color composite of the 14 January 1997 Landsat TM image. Also shown are USGS gauges at Gridley (11407150) and Nicolaus (11425000) for the Feather, Marysville (11421000) for the Yuba River, and Wheatland (11424000) for the Bear River. (b) Landsat image location.

Pall type A/E glass fiber filter with 1.0 μm nominal pore size.

[25] Above-water radiance was measured using an Analytical Spectral Devices (ASD) FieldSpec Pro (Boulder, Colo.), with a spectral range of 350–2500 nm. Total at-sensor radiance $L_t(\lambda)$, sky radiance $L_s(\lambda)$, and panel radiance $L_g(\lambda)$ were sampled using an 8° field-of-view foreoptic attached to the instrument. Before each water measurement we calibrated the ASD by referencing a diffuse, gray (nominally 10% reflecting) Spectralon panel (Labsphere, NH). All measurements were made at $\theta = 40°$ from nadir and at an azimuth directed $\varphi = 135°$ from the sun to minimize sun glint and instrument shading, and no more or less than 2 h from noon. Sky radiance was sampled by pointing the spectrometer directly toward the sky. At each site we obtained five replicate spectra of the panel, water surface, and sky radiance potentially reflected into the water-leaving radiance measurements. After checking and averaging each radiance measurement at a site, $E_d(\lambda)$ was determined from the measured panel radiance from equation (6) using the default proportionality factor (ρ, 0.028) for a wind speed under 5 m s^{-1} (Table 1), and clear sky conditions [*Mobley*, 1999]. Error introduced through variability in ρ was minimized by sampling at low wind speeds, and in a view direction that minimized sun glint and the effect of a nonuniform radiance distribution ($\theta = 40°$, $\varphi = 135°$) [see *Mobley*, 1999; *Toole et al.*, 2000]. Disruption of the water surface state and the resulting impact on the water-to-atmosphere transmission is more influenced by turbulence than wind speed on shallow, gravel-bedded streams [*Legleiter et al.*, 2004]. However, the lower Feather and Sacramento Rivers are both deep, sand-bedded rivers and we did not observe standing waves, or turbulence eddies, or wakes while sampling. Thus at these velocities and wind speeds, for our deep, sand-bedded rivers we used a flat-water value for ρ.

3.3. Optical Modeling

[26] Optical and radiative transfer modeling was then used to extend the field spectra to sediment conditions which existed during the two floods. Modeled spectra were only fitted to the measured spectra from the Sacramento River, as the panel measurements for the 16 February field day (on the Feather River) were unusable. A more detailed version of Figure 1 is given as Figure 4, and each step of our approach represented here by a box for a quantity, and a path for a process.
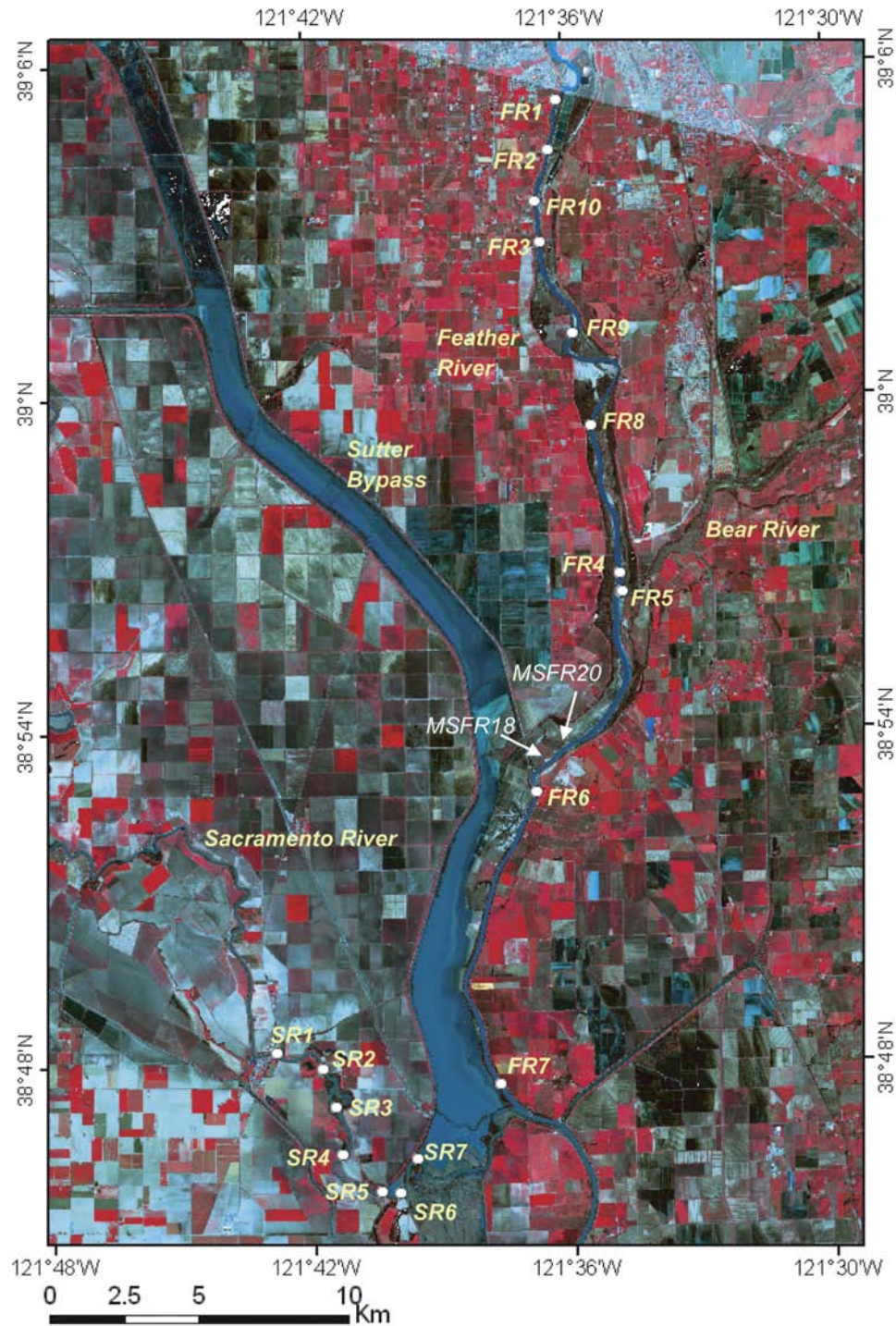
Figure 3. Sampling (yellow) and core (white) locations on the Sacramento and Feather Rivers over a 13 February 2006 SPOT image. SPOT is used only for showing the sampling locations because of the improved spatial resolution (10 m) over Landsat (30 m).

3.3.1. Mineral Optical Properties

[27] Mie equations require the spectral distribution of the relative refractive index (M) of the particle suspended in water (Figure 4, box a). Both the real (n_r) and imaginary (n') components of M were approximated as a homogenous population of clay minerals. Spectral values for compressed smectite (montmorillonite) pellets from Amory, Mississippi

are given by *Egan and Hilgeman* [1979]. Note that these measurements were made in reference to air. In order to apply these values to water, they were multiplied by the ratio of $n_{r\mathrm{air}}$ to $n_{r\mathrm{water}}$ at STP and 538 nm [*Bass et al.*, 1995], resulting in a n_r centered around 1.14. To test the sensitivity of the model to the refractive index, a low n_r of 1.124, and the n_r and density of quartz (1.148, 2.63×10^6 g m^{-3})

Table 1. Parameters for Mie Calculations and Hydrolight

Parameter	Value	Description
Relative refractive index, M	1.14	$n_r(\lambda)$ montmorillonite[a]
	0.001	$n'(\lambda)$[a]
Number-size distribution	$K = 10^{10}; j = -2$	Feather River core MSFR18 (60–62 cm)
Dmin, Dmax	0.05–30 μm	
Mineral density, ρ	2.5 Mg m^{-3}	montmorillonite[b]
Solar geometry	50.79° solar zenith	19.42 h UTC, on 15 Feb 2006, at 38°N, 121°W
Atmospheric conditions		
Sea level pressure	75.95 cm	default
Air mass type	10	continental
Relative humidity	66%	next three parameters from RADTRAN optimizing to field spectra
Precipitable water	1.2 cm	
Horizontal visibility	30 km	station at Sacramento Airport
24-h average wind speed	2.5 m s^{-1}	*Mobley* [1999]
L_r/L_s	0.028	
SSC, Cs	2–203 mg L^{-1}	
Pure water coefficients	a turn 20°C	*Pope and Fry* [1997]
$a_w(\lambda)$, $b_{B,w}(\lambda)$, $\beta_w(\theta)$		absorption
		Bukata et al. [1995]
		scattering
		Rayleigh-like phase function
CDOM, $a_{\mathrm{CDOM}}(d,\lambda)$	2.5 m^{-1} 400 nm	Exponential decay with d, λ[c]

[a][*Egan and Hilgeman*, 1979]; note that these were made in air. To convert to a water reference these values were multiplied by $n_{\mathrm{air}}/n_{\mathrm{water}}$ for pure water at STP and $\lambda = 538$ nm [*Bass et al.*, 1995].
[b][*Eshel et al.*, 2004].
[c][*Mobley*, 1994].

[*Wozniak and Stramski*, 2004] were also used to calculate the IOPs (Table 1, Figure 5).

[28] Few measurements exist in the visible spectrum of the imaginary index (n') for minerals relative to water. Here we used three values of n' in the Mie modeling—a constant n' of 10^{-3}, and a "medium" n' and "high" n' based on *Patterson et al.* [1977]. The medium value declines exponentially from 0.002 at 300 nm to 0.001 at 600 nm, and the high is the original data. For the modeled montmorillonite particles the constant n' of 10^{-3} appeared to be the most suitable, based on the resulting spectral shape (Figure 5).

3.3.2. Particle Size Distribution

[29] Sediment sampled in suspension in February 2006 was insufficient for determining the particle-size distribution because we are interested in this quantity during very large flood events; the low SSC conditions that existed while we were in the field would not translate to these high flows. Instead, we used several subsections of two cores taken from the floodplain of the Feather River as a proxy. Each core subsection was sieved to 250 μm and the remaining fines analyzed using a Micromeritics SediGraph III Particle Size Analyzer (Norcross, Georgia). Of these, we selected the most clay-rich sample (MSFR18 60–62 cm, 12.25%–71.56%–16.19% sand-silt-clay) to represent the size distribution of sediment suspended in the upper layer of river water. A particle density ρ_s, of 2.65 g cm^{-3}, settling in water with a density of 0.9939 g cm^{-3} and viscosity of 0.7136 mPas was used for all samples (Rolf Aalto, personal communication, 23 January 2008). Bins were defined logarithmetically from 1.09 to 325.5 μm. Since the SediGraph gives the mass size distribution, ρ_s was used to convert to equivalent spherical volumes, and from this a linear least-squares approximation to the SediGraph data was derived (see Appendix A for the details of how the mineral IOPs were determined), giving a slope (j) of −2, and a scale parameter (K) of 1.55×10^{10} (Table 1, Figure 4a). This satisfied the goodness-of-fit test of *Gaudoin*

et al. [2003] using correlation coefficients to test the hypothesis that a log-log plot of the number distribution fits a power law ($n = 69$, $r^2 = 0.999$, $\alpha = 0.01$).

3.4. Hydrolight

[30] A numerical solution to the general radiative transfer equation is implemented in the bio-optical model Hydrolight [*Mobley and Sundman*, 2001]. This model has been extensively tested, accurately reproducing in situ R_{rs} measurements in turbid rivers, coastal waters, and lakes [e.g., *Bergmann et al.*, 2004; *Brando and Dekker*, 2003; *Green and Sosik*, 2004]. A three-component model was used, parameterized with the values listed in Table 1.

[31] In Hydrolight the inputs can be divided into those which define the inherent optical properties of the water body (Figures 4a–4c), and those which define the radiometric conditions (Figures 4d–4f). For the first, pure water, color dissolved organic matter (CDOM), and mineral particles were included to form a three-component model. Algae and other photosynthetic species were not observed in the cold water of the Feather River. Each inherent optical property can then be determined by summing the individual contributions, i.e., for absorption:

$$a(\lambda) = a_w(\lambda) + a_{\mathrm{CDOM}}(\lambda) + C a_m^*(\lambda), \qquad (8)$$

where the first component $a_w(\lambda)$ represents absorption by (chemically) pure water [see *Bukata et al.*, 1995], the second $a_{\mathrm{CDOM}}(\lambda)$ by CDOM, and the third $a_m^*(\lambda)$ by mineral particles. Scattering and backscattering are then similarly expressed for water and mineral particles.

[32] Pure water coefficients were taken from the literature for absorption [*Pope and Fry*, 1997] and scattering [*Bukata et al.*, 1995, p. 119] with a Rayleigh-like scattering phase function. Mineral coefficients were determined theoretically as described in section 3.3.1, and the mineral scattering phase function was determined for each wavelength
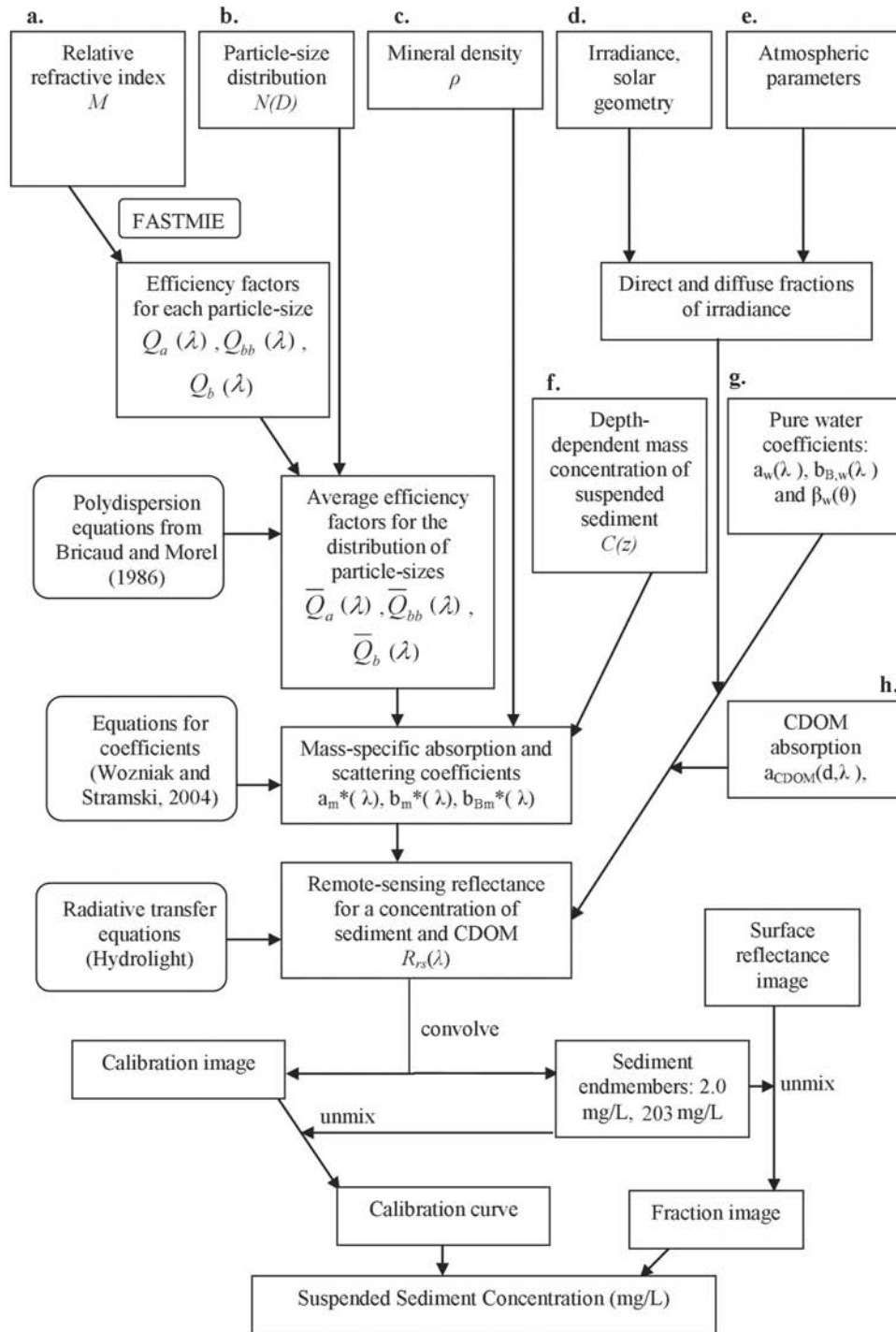
Figure 4. Modeling approach for deriving suspended sediment concentrations (a–h in Table 1).

from the theoretical backscattering to total scattering fraction and a Fournier-Forand phase function with a tolerance of 0.005 [see *Mobley and Sundman*, 2001].

[33] Consistent with the use of optical cross sections to describe photon interactions with each component, the specific mineral coefficient (a_m^*) is expressed in units of area per unit mass ($m^2 g^{-1}$). When multiplied by the suspended sediment concentration SSC ($g m^{-3}$), this gives the attenuation through a path length (m^{-1}). Therefore specific coefficients for the mineral particles were obtained by multiplying the

theoretical coefficients by the SSC at the water surface, estimated as the depth of optical penetration (0.25 m).

[34] A simple model for CDOM dependence on depth and wavelength was used to generate several $a_{CDOM}(\lambda)$ spectra (m^{-1}), which were then added to the theoretical mineral absorption. Referenced to 440 nm:

$$a_{CDOM}(\lambda, d) = a_{CDOM}(440, 0)^* \exp(-d/5)^* \exp[-\gamma^*(\lambda - 440)],$$

$$(9)$$
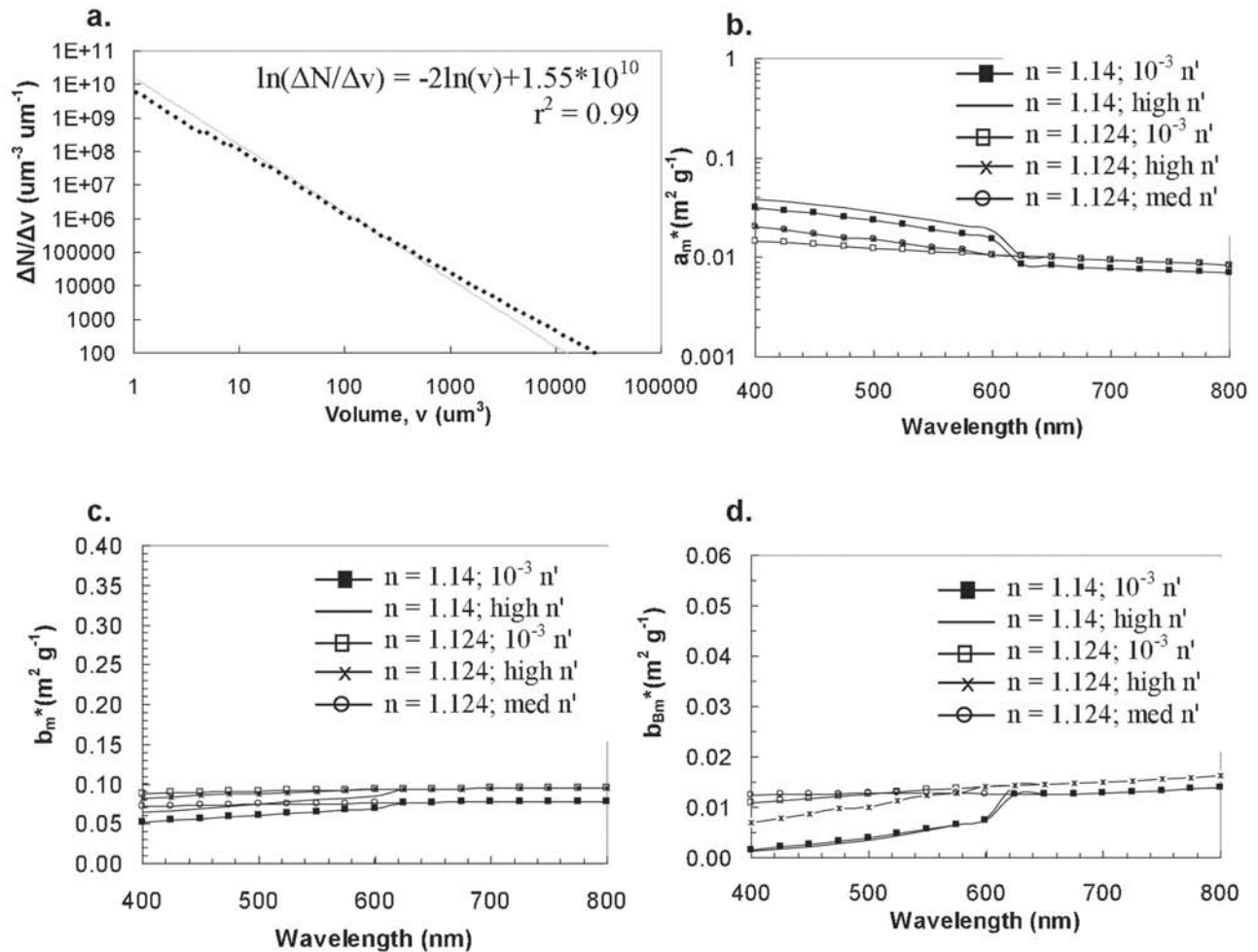
Figure 5. Optical model parameters. (a) Power law fit to the number size distribution of core MSFR18 (60–62 cm) from the Feather River floodplain. Location of core shown in Figure 2. (b) Effect of the real part n_r and the imaginary part n' of the refractive index on the modeled mass-specific absorption coefficient. The high and medium n' are based on the data of *Patterson et al.* [1977]. For each, the values decline exponentially from a wavelength of 300 nm ($n' = 0.01;0.002$) to a wavelength of 600 nm ($n' = 0.002;0.001$) and are constant thereafter. A slope of $j = -2$ was used for all cases. (c) and (d) as for (b) but for (c) the mass-specific scattering coefficient and (d) backscattering coefficient. A montmorillonite (1.14) with a 10^{-3} n' was used to model the Feather River sediment (see text for details).

where γ is a slope parameter which has been observed to vary from 0.011 to 0.021 due to a difference in contributions by fulvic and humic acids [*Bukata et al.*, 1995], and d is depth (m). We used a γ of 0.014 m^{-1} based on mean values from Australian inland waters [*Kirk*, 1994; *Mobley*, 1994]. The reference absorption $a_{CDOM}(440,0)$ was then varied from 0.4 to 4 m^{-1} (Figure 6).

[35] Radiometric conditions were selected to match the lighting and atmospheric state near noon (19.42 UTC) on the first day of the field campaign (Table 1). Hydrolight accepts a total incident irradiance from the user—then partitions it into a diffuse E_d(diffuse) and direct E_d(direct) component using a coupled atmospheric model, RAD-TRAN [*Gregg and Carder*, 1990]. RADTRAN was parameterized using values for the relative humidity (66%), precipitable water (1.2 cm), and horizontal visibility (30 km), which optimized the fit between L_s near noon measured in the field on 15 February 2006 at 38°N, 121°W,

and the L_s obtained from RADTRAN (Table 1). Although RADTRAN was developed for maritime atmospheres, the partitioned sky radiance matches the field measurements well with a visibility of 30 km, except below 450 nm where mineral particles have little impact. A complete radiance distribution was then computed for clear conditions using the *Harrison and Coombes* [1988] semianalytic model. With these parameters, and accepting some assumptions about the transfer of upwelling light across the water surface, the radiative transfer equations were solved in Hydrolight, yielding $R_{rs}(\lambda)$ for a specific SSC and CDOM level. Hydrolight assumes a plane-parallel water body of infinite horizontal extent, and we assumed an infinite vertical extent below 3 m based on calculations of the diffuse attenuation coefficient, $K_d(z,\lambda)$, with a SSC of 2.0 mg L^{-1} and the atmospheric parameters for 15 February 2006 (Table 1).

[36] In order to determine the depth at which there is nearly complete extinction of the incident light, we calculated
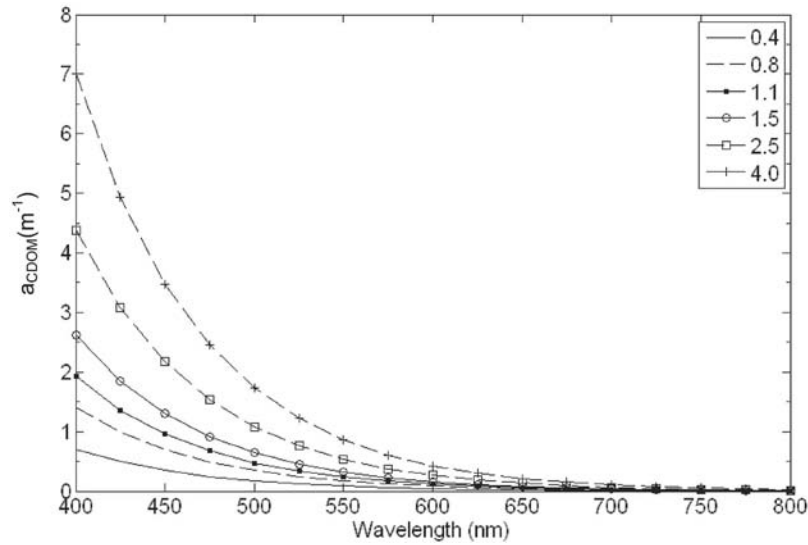
Figure 6. Spectral absorption coefficients. Each line is for an absorption coefficient (m^{-1}) of color dissolved organic matter (CDOM) at a reference wavelength of 440 nm, and shows the decay in absorption with increasing wavelength. These spectra were added to the mineral absorption coefficients to model the remote-sensing reflectance (R_{rs}) in Hydrolight.

values of $K_d(z,\lambda)$ with the lowest expected SSC (2.0 mg L^{-1}) and for a wavelength of 650 nm, with the least absorption by water within our range of interest. Using the Beer-Lambert law describing the attenuation of light through a medium, we could then obtain the depth at which less than ~1% of the light intensity remains [*Kirk*, 1994]. This gives us the maximum expected optical depth, z (0.25 m) for these conditions.

[37] Finally, $R_{rs}(\lambda)$ was converted to water-leaving reflectance, $R(\lambda)$ (unitless) to create an end-member library for unmixing the atmospherically corrected Landsat images. This step is required in order to obtain the same units as is measured at the top of the atmosphere. Irradiance reflectance $R(\lambda)$ is related to $R_{rs}(\lambda)$ by a ratio $Q(\theta,\varphi,z = 0,\lambda)$ defined just below the water surface:

$$Q(\theta,\varphi,z = 0,\lambda) \equiv \frac{E_u(z = 0,\lambda)}{L_u(\theta,\varphi,z = 0,\lambda)}, \qquad (10)$$

where $E_u(z = 0,\lambda)$ is the upward (water-leaving) irradiance (W m^{-2} nm^{-1}), divided by the upward directed radiance $L_u(\theta,\varphi,z = 0,\lambda)$. Both $E_u(z = 0,\lambda)$ and $L_u(\theta,\varphi,z = 0,\lambda)$ were determined in Hydrolight, and $R(\lambda)$ defined as the product of $R_{rs}(\lambda)$ and $Q(\theta,\varphi,z = 0,\lambda)$ along a path perpendicular to the water surface.

3.5. Inverse Modeling

[38] Forward modeling in Hydrolight generated a set of R_{rs} spectra which could then be statistically compared to the field measurements in order to estimate $a_{CDOM}(440,0)$. The criterion for the best fit was the least-square distance (D) computed between the modeled $R_{rs}(\lambda)_{Hydrolight}$ and measured spectra $R_{rs}(\lambda)_{ASD}$ with 65.9 and 96.5 mg L^{-1} SSC:

$$D = \sum_{\lambda} [R_{rs}(\lambda)_{ASD} - R_{rs}(\lambda)_{Hydrolight}]^2. \qquad (11)$$

There is a considerable amount of variability associated with the field measurements of SSC/R_{rs} (Figure 7). These two SSC levels bracket a best fit (65.9 mg L^{-1}) based on

the shape of the model spectra conforming to the shape of the field spectra, and then a fit to the highest measured SSC (96.5 mg L^{-1}). By the first criteria, $a_{CDOM}(440,0)$ was set to 2.5 m^{-1}, with an RMSE (in % reflectance) of between 0.0304% and 0.0437% (at 65.9 and 96.5 mg L^{-1}, respectively). Using this $a_{CDOM}(440,0)$, a set of R_{rs} spectra were modeled for suspended sediment concentrations ranging from 2 to 203 mg L^{-1} (Figure 8).

3.6. Image Analysis

[39] Landsat MSS and TM data were acquired for floods on 21 March 1986 and 14 January 1997, respectively. Three preprocessing steps were required in order to obtain absolute surface SSC values in milligrams per liter—geolocating and atmospherically correcting the images, and subsequently applying a mask to exclude areas not clearly inundated. All data sets were reprojected to UTM Zone 10N, WGS84 datum. Images were analyzed using linear mixture analysis after applying a mask generated using low values from a ratio of the green to near-infrared bands. Finally, a look-up table was applied to convert the end-member fractions to SSC, and the error assessed. Details of the atmospheric correction of the Landsat images and the conversion to ρ_w are given in the Appendix.

[40] The two selected end members derived from Hydrolight represent R spectra with a given concentration of suspended sediment—a low SSC of 2 mg L^{-1} and a high of 203 mg L^{-1}—and CDOM absorption (Figure 8). Mixture equations were solved using these end members and an unconstrained, singular value decomposition implemented in VIPER Tools [*Roberts et al.*, 2007] and ENVI (RSI). Reflectance spectra from Hydrolight, convolved to fit each sensor band pass, were then analyzed using linear mixture analysis to derive the fractions reported in the calibration curves shown as Figure 9. These values have been scaled such that a fraction of 0% is equal to a DN of 100 and a fraction of 100% is equal to a DN of 200. Although the
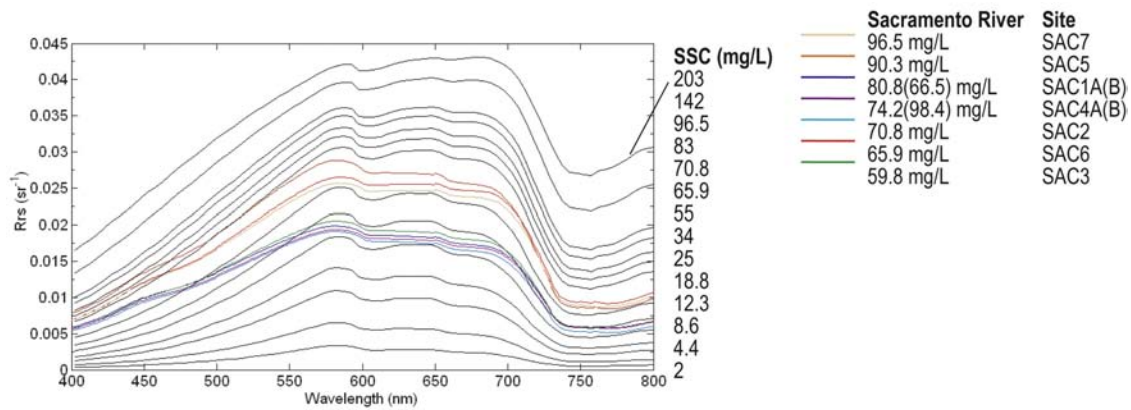
Figure 7. Remote sensing reflectance (R_{rs}) for a range of sediment concentrations (mg L^{-1}) suspended in the Sacramento River. Shown for comparison are the spectra resulting from optical and radiative transfer modeling in Hydrolight (black), and computed from measured radiance (color) using an Analytical Spectral Devices (ASD) FieldSpec Pro (Boulder, Colo.) with a spectral range of 350–2500 nm and an 8° foreoptic. Samples shown here were collected on 15 February 2006, at the locations shown in Figure 2 on the Sacramento River.

calibration curve is extended slightly beyond a DN of 200, we could only classify pixels with DNs > 200 as greater than our maximum end-member value (203 mg L^{-1}). Finally, a look-up table was generated to relate the fraction values for the Feather River images to absolute values of surface SSC in milligram per liter.
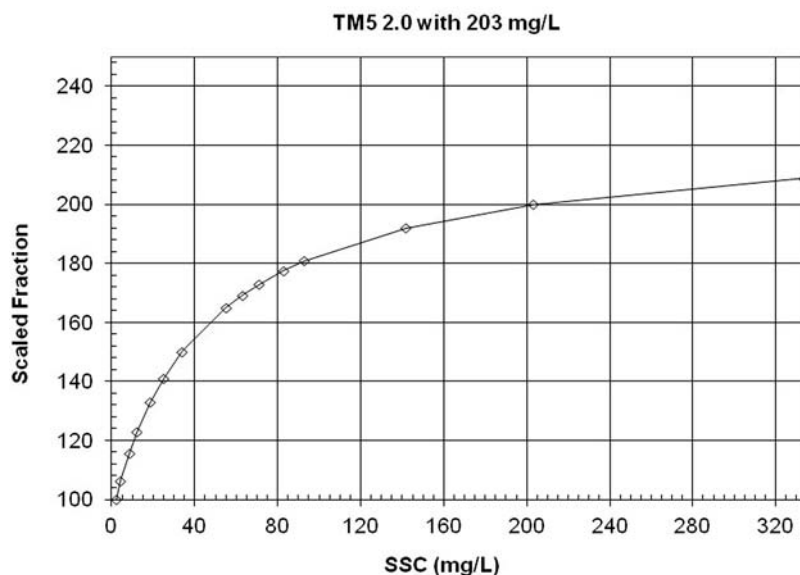
4. Results

[41] Little sediment is released by Oroville Dam (Figure 1) and concentrations are generally low directly downstream of the reservoir. However, mobilization of dredge mining spoils between Oroville Dam and Marysville is apparent in moderate levels of SSC ranging from 40 to 120 mg L^{-1} in 1986 (Figure 10) and 20 to over 60 mg L^{-1} in 1997 (Figure 11). By 56.3 km upstream from Verona (the confluence of the Feather and Sacramento Rivers), concentrations drop to between 30 and 80 mg L^{-1} in 1986, and then by half in 1997 (10–30 mg L^{-1}), then increase again with relatively high contributions from the Yuba River. During the 1997 New Year's flood, the greatest sediment load was transported by this tributary. Below Marysville, contributions from the Yuba River caused an increase in the washload to 50–130 mg L^{-1} in 1986 while the concentrations in
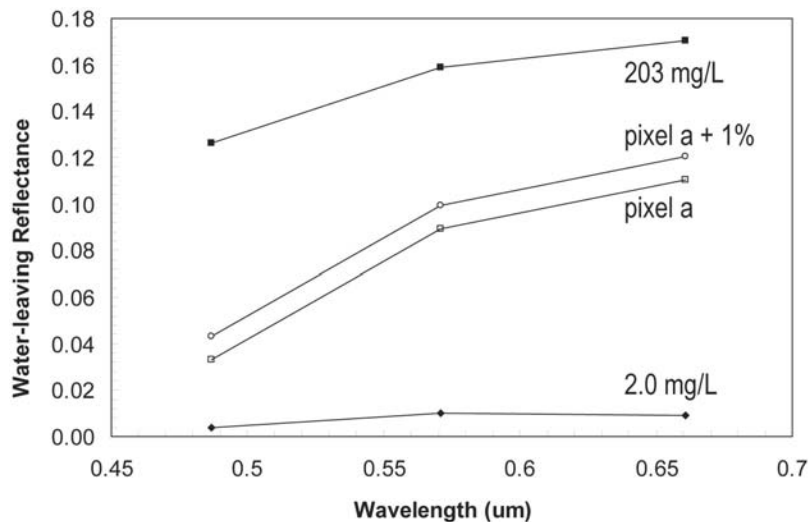
Figure 8. Water-leaving reflectance (R) for two end members used in the spectral mixture analysis (2 and 203 mg L^{-1}). Spectra were derived from optical and radiative transfer modeling in Hydrolight and convolved to fit the Landsat TM sensor band-pass for the first three visible bands. Modeled spectra are for montmorillonite ($n_r = 1.14$) with a 10^{-3} n', an $a_{CDOM}(440,0)$ of 2.5 m^{-1}, and a PSD slope (j) of -2 (see text for details). Also shown are pixel R values for a water-sediment-CDOM mixture taken from the 1/14/97 Landsat image of the Feather River, and the same pixel with a hypothetical increase of 1% in the reflectance in order to show the impact of a 10 km difference in the visibility parameter used to model path radiance in MODTRAN.

Figure 9. Calibration of spectral mixture analysis results to surface sediment concentrations. The fraction values from the sediment-water fraction image are converted to suspended sediment concentrations (mg L^{-1}) using the above relationship. These curves are taken from Hydrolight generated spectra, based on the inversion of field spectra from the Sacramento River and convolved to fit Landsat TM5 bandwidth specifications for the expected range of concentrations.

1997 were about the same. Suspended sediment loads decrease on the Yuba below Englebright Dam (10 to >210 mg L^{-1}), across the gold fields to the confluence with the Feather (10–120 mg L^{-1}). Concentrations in the Feather drop again below a crevasse where sediment was deposited into the Sutter Bypass, so that by 12 km above Verona SSC is 20–50 mg L^{-1} (Figure 10). Clearer backchannels and ponded floodplain water range from 0 to 40 mg L^{-1}.

[42] In Figure 12 our field measurements and the surface modeled SSCs are plotted against other field samples acquired near the USGS gauge at Nicolaus (Figure 1) covering a span of three years (1996–1998). The model data fall within the envelope of field samples; however, the model underpredicts the concentration at Nicolaus in 1997 at the time of the image acquisition by up to 80 mg L^{-1}.

5. Discussion and Error Analysis

[43] There is increasing interest in the fluvial community in using physically based models to interpret hydrologic parameters from remote sensing data [*Marcus and Fonstad*, 2010]. Our field samples exhibited the same problems that make it difficult to produce quality empirical relationships between SSC and R_{rs}. Field data sets relating suspended sediment concentration to R_{rs} are limited by the difficulty in capturing the full range of optical conditions which can exist in the water body, and by the nonlinear response of R_{rs} to SSC (Figure 9). In addition, this response depends on the character of suspended sediment—in particular, the particle-size distribution—and is affected by the presence of dissolved organic matter. Here we formulate an approach that is based upon the physics of the problem of inferring water quality parameters remotely. We are able to do so because of recent advances in computer processing capabilities and the numerical solutions to complex radiative trans-

fer equations. We hope that we have presented a coherent structure for translating information about the mineralogy and particle-size distribution of sediment transported in suspension to maps of suspended sediment concentrations. At this point however, there are still many uncertainties in the input model parameters, and we were not able to achieve particularly good model closure. However we are able to quantity the sources of error arising from this approach given our assumptions, and discuss these errors in section 5.1 in order to inform future efforts toward building a physically based model relating SSC and R_{rs}.

5.1. Accuracy Assessment

[44] The final accuracy of this approach depends upon the sum of the errors at each step in the image transformation processes and on the suitability of the end members. Table 2 summarizes the impacts on SSC (increasing or decreasing) of overestimating the principle model parameters. Error arising from converting the image DNs to R is primarily driven by the uncertainty in the atmospheric modeling; this conversion is especially difficult over water where the returned signal is low. To test the impact of the modeled path radiance (see Appendix) on the resulting sediment concentrations, MODTRAN (moderate spectral atmospheric resolution transmittance algorithm and computer model) [*Berk et al.*, 2003] was run with a visibility—a surrogate for the aerosol concentration—of 20 and 30 km. A 10 km decrease in the visibility parameter had no impact on low SSCs (<50 mg L^{-1}), but reduced the predicted SSC by 10 mg L^{-1} at higher concentrations.

[45] Conversion to SSC includes error from the mixture analysis which is explicitly known from the residuals, and from the reflectance spectra used as end members. All of the RMS errors were well under 0.03, translating into ≪10 mg L^{-1} impact on the predicted SSC. In addition,
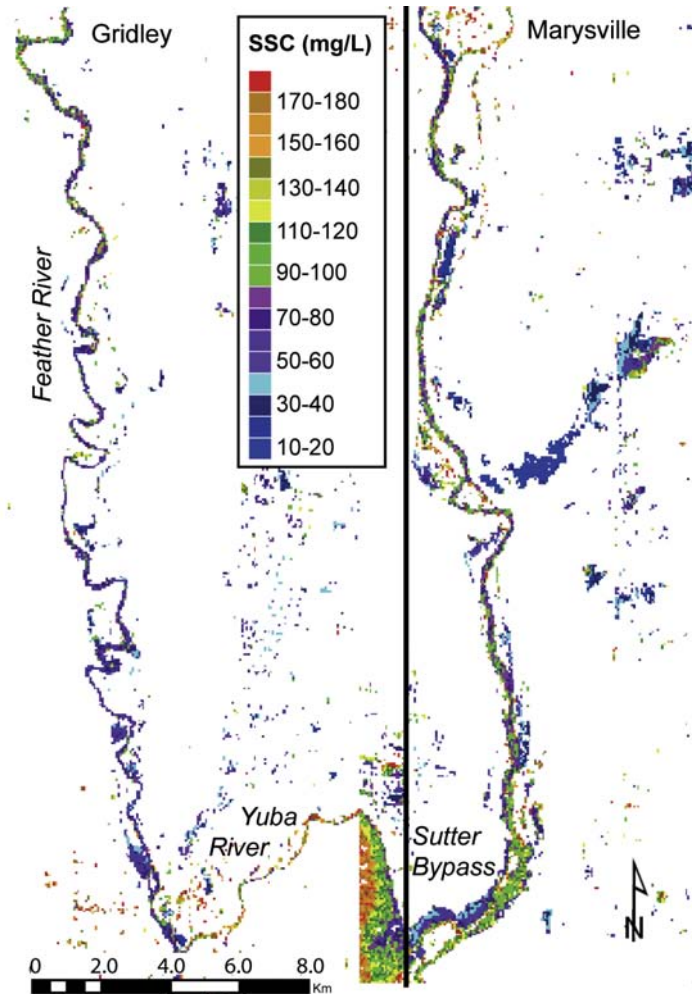
Figure 10. Surface sediment concentrations (mg L^{-1}) of the Feather River on 21 March 1986. Left panel is from Gridley to Marysville, and the right panel is from Marysville to the Sutter Bypass. Concentrations were derived using the look-up table in Figure 9 to convert end-member fractions from a spectral mixture analysis. A two-end-member model was used, with synthetic end members derived from optical and radiative transfer modeling in Hydrolight, and inversion of field spectra from the Sacramento River to estimate $a_{CDOM}(440,0)$. The high end member was 203 mg L^{-1}, and the low 2.0 mg L^{-1}.

there were no negative or superpositive (>100%) values in the rivers, suggesting that the model end members are appropriate.

[46] Several assumptions went into modeling the end members. In order to assess the impact of these assumptions, the most sensitive parameter values were varied over a plausible range. Errors in n_r are primarily manifested

Table 2. Summary of Impacts From Overestimating the Primary Model Input Parameters on SSC

Parameter	Impact of Overestimating on SSC
Path radiance, $L_{path}(\lambda)$ estimated using visibility	+
Number-size distribution, j	−
Real refractive index, $n_r(\lambda)$	+
Imaginary refractive index, $n'(\lambda)$	+
CDOM, $a_{CDOM}(d,\lambda)$	−

in b_{bmin} (Figure 5d), while errors in n' dominate the a_{min} spectrum (Figure 5b). The particle-size distribution may be biased toward larger particles because the sample was obtained from a floodplain core. Thus R_{rs} was also modeled with a steeper slope parameter ($j = -4$), typically applied to distributions of suspended particles in the ocean. Given a SSC of 70.8 mg L^{-1}, this slope parameter increased R_{rs} by 4.68% at the peak (588 nm) relative to the core-derived slope, translating to a 20 mg L^{-1} decrease in the predicted SSC. However, the field samples and the set of image results suggest that an under-prediction of SSC is more likely (Figure 12). Furthermore, recent work establishing the size distribution of inland water mineral particle reports a much coarser size distribution (average $j = -2.8$) than the typically assumed Junge slope (j of −4) of marine detrital particles [Peng et al., 2007]. Also, the magnitude of the predicted b_m^* falls within the measured range for several coastal and shelf marine environments, which are close to or <0.5 m^2 g^{-1} in the green part of the spectrum [Babin
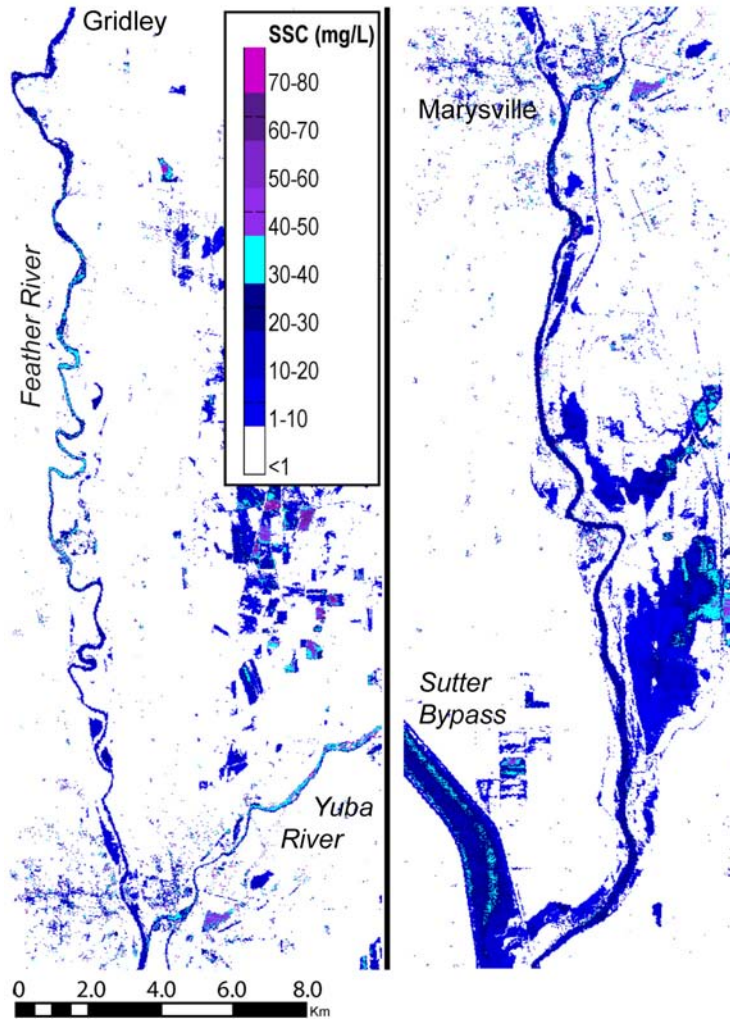
Figure 11. Surface sediment concentrations (mg L^{-1}) of the Feather River on 14 January 1997.

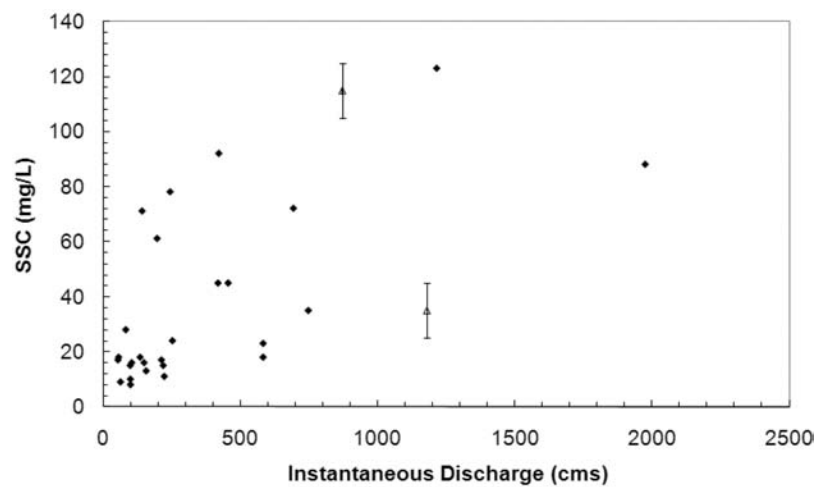**Figure 12.** Comparison of field samples (black diamonds) of surface sediment concentrations (SSC, mg L^{-1}) from the USGS at the Nicolaus gauge station (1996–1998) to concentrations derived from the March 1986 and January 1997 Landsat images (open triangles). See Figure 3 for gauge location. Note that the error bars represent the accuracy of the look-up table, and are not representative of the cumulative error.

et al., 2003; *Bowers and Binding*, 2006; *Wozniak and Stramski*, 2004]. Consequently, it is unlikely that the chosen slope resulted in overprediction of SSC.

[47] *Wozniak and Stramski* [2004] report a range of n_r values for minerals commonly suspended in seawater. The lowest clay value (1.124) was used to test the impact on SSC estimation, in keeping with the assumption that the bias in the modeled spectrum is toward R_{rs} values that are too high. If n_r was overestimated by as much as 0.016, the peak R_{rs} was overestimated by only 0.14% for a SSC of 70.8 mg L^{-1}. Increasing the mineral absorption to the high n' values has an even smaller impact on R_{rs} (−0.04%). Both changes to the refractive index would increase the image SSC values by between 4 and 40 mg L^{-1}, with a greater impact at higher concentrations. However, changing the refractive index also alters the R_{rs} spectral shape. Overall, the shape of the modeled spectra with the chosen refractive index better matched the two field spectra used to fit the parameters. In addition it is unlikely that n' exceeds 10^{-3}, as the few measurements which do exist for clays suspended in water give this as an upper bound [*Gillespie et al.*, 1974]. However, it is possible that the Feather River transports soil high in strongly absorbing iron oxides [*Sokolik and Toon*, 1999; *Stramski et al.*, 2007], driving a greater value for n'.

[48] These contradictory tendencies illustrate the difficulty of this approach, as it appears that a range of mineral parameters (i.e., particle size, mineralogy) can produce similar R_{rs} spectra. Furthermore, real nonspherical and internally heterogeneous soil particles have complex absorption and scattering centers. For example, iron, which is a major pigmenting agent, can occur as a surface coating or an element of mineral lattice, or it can form crystals of oxides. These soil particles can have an order-of-magnitude greater a_m depending on the size distribution since smaller particles are more absorbing [*Stramski et al.*, 2007].

[49] With this constraint, the predicted error associated with the estimated SSC for the images is on the order of 15–25 mg L^{-1}. Further work is required to better establish the optical properties of suspended sediment, however field measurements of suspended sediment concentrations are rarely more accurate [*Meade*, 1985].

5.2. Inversion and Dissolved Organic Carbon

[50] This approach requires a unique solution to a combination of inherent optical properties and boundary conditions, and the accuracy of the SSC retrieval depends on how well CDOM is parameterized. Two field R_{rs} spectra were used to constrain the inversion problem. However our field data illustrate the difficulty in acquiring precise empirical relationships between high levels of SSC and R_{rs}, potentially explaining why so few empirical relationships exist for rivers with high levels of suspended sediment. Temporal and spatial variability in the suspended sediment transported by the Sacramento and Feather River resulted in a difference of up to 7% between SSC replicates, and of 20–30 mg L^{-1} for indistinguishable field spectra. For example, the R_{rs} associated with the 65.9 mg L^{-1} sample also could have been up to 96.5 mg L^{-1} (Figure 7).

[51] The uncertainty in the field measurements translates into the inferred CDOM level; however the CDOM estimate from the inversion appears reasonable. Based on data from 2000 to 2002 collected near the gauge at Nicolaus, the

concentrations of dissolved organic carbon (DOC) do not vary with the total suspended load, and are relatively constant downstream from Oroville Dam (station A5519100) to Verona (station A51010.50; http://waterdata.usgs.gov). Concentrations show a slight seasonal trend, increasing during periods of rising water in the winter such that the total range is 1.2–4.2 mg L^{-1} DOC for this period at Verona. This gives a likely upper bound to the DOC concentration during the 1997 flood; the peak at Nicolaus was greater (11.36 m) than when the high (4.3 mg L^{-1}) measurement was taken. DOC concentrations are generally about half the dissolved organic matter by weight, and are on average near 9 to 10 mg L^{-1} in inland waters [*Bukata et al.*, 1995].

[52] Observations of $a_{CDOM}(440, 0)$ in rivers range from 0.44 m^{-1} for the Molonglo River in Australia to 12.44 m^{-1} for the Carrao in Venezuela [*Kirk*, 1994]. Applying an $a_{CDOM}(440, 0)$ of 4.0 m^{-1} to Hydrolight lowered the peak R_{rs}, compared to an $a_{CDOM}(440, 0)$ value of 2.5 m^{-1}, by 0.002 sr^{-1}, translating to an increase of ∼20 mg L^{-1} around a SSC of 70 mg L^{-1}. However, this also places the peak reflectance at 647 nm. With $a_{CDOM}(440, 0)$ at 2.5 m^{-1}, R_{rs} peaks at 587 nm; this is much more consistent with the field measurements (R_{rs} peak 585 nm). Again, it is important to note the impact of varying these parameters on the spectral shape.

[53] Since only one measurement exists for the 1997 flood, and none for the 1986 event, it is not possible to explicitly assess the accuracy of applying this calibration to flood conditions. The image-derived 1997 values are low (up to ∼35 mg L^{-1}, Figure 12), suggesting the reflectance of the end member associated with a particular SSC was too high. In fact, as discussed above, many of the uncertainties in this approach would produce a positive error, i.e., R being too bright (Table 2).

6. Conclusions

[54] On many rivers, studies of suspended sediment transport are constrained by the lack of SSC measurements, especially during floods. Since the 1970s, the ability to retrieve these concentrations from remotely sensed imagery has opened up the possibility for reconstructing past transport conditions. Unfortunately there is still a great deal of uncertainty in the relation between the water-leaving reflectance and these concentrations in turbid, inland water bodies, because, in part, of the impact that different particle sizes and mineralogy have on scattering properties. This impact is addressed here by considering the number-size distribution of the sediment in transport during floods on the Feather River, and assigning a mineralogy to the sediment in order to model the contribution by suspended mineral particles to the inherent optical properties of the river water. Furthermore, the dissolved component of organic matter was estimated using an inversion of a field data set.

[55] Most of the errors from the approach would produce at most ∼10 mg L^{-1} difference in the predicted SSC. However, temporal and spatial variability in SSC resulted in field spectra with SSC differences of up to 30 mg L^{-1}, and an inaccurate n_r resulted in an under-estimate of up to 40 mg L^{-1} at SSC levels >50 mg L^{-1}. Since the approach is only as good as the field measurements, an improved

calibration could be achieved by more extensive sampling so that the fit is better constrained. Alternatively, if CDOM absorption is measured in the field, the calibration would depend less upon field measurements of SSC, which as discussed in section 1 often cannot be acquired during flood conditions. Overall the modeled reflectance closely followed the shape of the field spectra, and predicted similar concentration ranges and patterns as field measurements of SSC. Therefore this method shows promise for deriving past flood concentrations using water and sediment properties from current, lower flow conditions.

Appendix A: Determination of Mineral IOPs

[56] In order to obtain the mass-specific absorption and scattering coefficients (IOPs) for the suspended sediment, as required by Hydrolight, we first solved the Mie equations of *Bohren and Huffman* [1983] coded in FASTMIE (http://misclab.umeoce.maine.edu/software.php) to obtain efficiency factors $Q_a(\lambda)$, $Q_B(\lambda)$, $Q_b(\lambda)$ for *each* particle size. Following the methods of *Bricaud and Morel* [1986], *bulk* average efficiency factors $\overline{Q}_{x=a,b,B}(\lambda)$ were then calculated for the spectral range where the signal of mineral particles suspended in water dominates ($\lambda = 400$–800 nm).

[57] In order to determine the bulk average efficiency factors, a particle-size distribution is needed. From theoretical work, the particle-size distribution of suspended fine sediment can be approximated by a power law (Junge-type) size distribution [*Bader*, 1970, equation (2)], where

$$N(x) = k \left(\frac{x}{x_0}\right)^{-m} \tag{A1}$$

and $N(x)$ is the number of particles in the mixture volume of a size x, x_0 is a reference size (usually set to unity), and k and m are coefficients describing the distribution shape. This distribution function is valid when very small particles have a negligible volume and the number of the largest particles is negligibly small. For Mie computations of polydisperse systems, the *number* size distribution is more relevant than the *cumulative* distribution given in equation (A1). Thus, where the size parameter is the volume (v replaces x), the number of particles in the size interval from v to $v + dv$ can be written as

$$\left|\frac{dN(v)}{dv}\right| = kmv^{-(m+1)} \equiv Kv^{-j}. \tag{A2}$$

[58] Bulk average efficiency factors were determined by weighting the individual factors for each diameter i by the particle-size distribution via

$$\overline{Q}_x(\lambda) = \frac{\int_{Dmin}^{Dmax} Q_i(\lambda, D) K D^j D^2 dD}{\int_{Dmin}^{Dmax} K D^j D^2 dD}, \tag{A3}$$

where D is the particle size of the mineral. The limits to the above equation (D_{min} and D_{max}) were set to capture the range of the most optically significant mineral size fraction, and thus D_{max} was set low, at 30 μm, while D_{min} was set at half the SediGraph detection limit (0.05 μm, Table 1).

[59] From this and a mineral density the model IOPs of the suspended particle mixture were calculated using the approach of *Wozniak and Stramski* [2004]:

$$x_m^*(\lambda) \equiv \frac{3\overline{Q}_x(\lambda)}{2\rho_s} \frac{\int_{Dmin}^{Dmax} K D^j D^2 dD}{\int_{Dmin}^{Dmax} K D^j D^3 dD}, \tag{A4}$$

where $x = a$, b, or b_B [*Bricaud and Morel*, 1986] and ρ_s is the mineral density.

Appendix B

B1. Landsat Image Calibration and Atmospheric Correction Image Calibration

[60] Conversion from the calibrated and quantized scaled radiance (QCAL) in digital numbers to radiance L_λ (W m^{-2} sr^{-1} μm^{-1}) is given by

$$L_\lambda = G \times QCAL + B \tag{B1}$$

with the following gains (G) and offsets (B) for MSS 5 and TM 5.

[61] A modified approach was adopted for radiometric calibration of the L5 TM sensor in order to account for degradation in the internal calibration lamps over time. Now calibration is implemented using a time-dependent look-up table generated from the lifetime gain equations [*Teillet et al.*, 2001], a cross calibration with the Landsat 7 Enhanced Thematic Mapper Plus, and the instrument's response to pseudo-invariant desert sites [*Chander et al.*, 2007]. Furthermore, biases are applied line-by-line (rather than by scene) based on the dark shutter responses acquired from each scan line, and the regression based offset discarded. These changes bring the L5 calibration into line with the L7 ETM + protocol.

[62] Conversion to L_λ (W m^{-2} sr^{-1} μm^{-1}) is then given by

$$L_\lambda = G_{rescale} \times QCAL + B_{rescale}, \tag{B2}$$

where

$$G_{rescale} = \frac{LMAX_\lambda - LMIN_\lambda}{QCAL_{max}}, \tag{B3}$$

$$B_{rescale} = LMIN_\lambda, \tag{B4}$$

and $QCAL_{max}$ is the maximum quantized calibrated pixel value. $LMIN_\lambda$ and $LMAX_\lambda$ are the spectral radiances (W m^{-2} sr^{-1} μm^{-1}) for each band at a digital number of 0 and 255 ($QCAL_{max}$) respectively. Gains ($G_{rescale}$) and offsets ($B_{rescale}$) were defined by the post-calibration dynamic range ($LMIN_\lambda$ and $LMAX_\lambda$) given in Table B1 for L5 images acquired after 5 May 2003 [*Chander et al.*, 2007].

B2. Atmospheric Correction

[63] Atmospheric correction is generally performed by modeling the path radiance (ρ_{path}) and transmittance (τ) of the atmosphere at the time and location that the image was

Table B1. Radiometric Calibration Coefficients

| Band | MSS 5 | | TM 5 | |
| | Gain | Offset | $LMIN_\lambda$ | $LMAX_\lambda$ |
	(W m^{-2} sr^{-1} μm^{-1})		(W m^{-2} sr^{-1} μm^{-1})	
1	2.086610	3.0	−1.52	193.0
2	1.385830	3.0	−2.84	365.0
3	1.125980	5.0	−1.17	264.0
4	0.944882	3.0	−1.51	221.0

acquired using radiative transfer algorithms. We applied MODTRAN v. 4.3 (moderate spectral atmospheric resolution transmittance algorithm and computer model), an updated version of LOWTRAN, developed by the Air Force Research Lab, Space Vehicles Directorate, in collaboration with Spectral Sciences, Inc [*Berk et al.*, 2003] to calculate the atmospheric transmittance, background atmospheric radiance, single-scattered solar radiance, multiple-scattered solar radiance, and direct solar irradiance [*Bukata et al.*, 1995]. MODTRAN requires inputs of the time, date, and location of image acquisition, satellite elevation, mean scene elevation, water vapor content, an estimate of the *visibility* which is used to estimate the aerosol content, and a generic atmospheric mode (see Table 1). Generic atmospheric models are necessary for analyzing imagery where the meteorological conditions were not recorded, as is often the case with historic imagery.

[64] Once the data were calibrated and converted to radiance, an atmospheric correction could be applied using the MODTRAN 4 radiative transfer code run in ACORN (atmospheric correction now). Inputs specific to the sensor and solar geometry at the time of acquisition, 10 mm of atmospheric water, and a mean elevation of 156 m were used for all images (Table 1). A mid latitude winter atmosphere was applied to the TM 5 image with a 30 km horizontal visibility parameter to estimate the aerosol content of the atmosphere. However a lower visibility (20 km) parameter, and a mid latitude summer atmospheric model was used for the MSS image to account for the change in atmosphere during the spring in the Sacramento Valley. Visibility was set to minimize reflectance in deep, clear water bodies in the image, and was kept within the range of visibility measured on those days at the Sacramento Airport (http://cdo.ncdc.noaa.gov/CDO/cdo).

References

Albanakis, K. S. (1990), Testing of a model for the simulation of the volume reflectance of water due to suspended sediment under controlled conditions, for various sediment types, *Int. J. Remote Sens.*, *11*(9), 1533–1547.

Austin, R. W. (1980), Gulf of Mexico, ocean-color surface-truth measurements, *Boundary-layer Meteorol.*, *18*, 269–285.

Babin, M., A. Morel, V. Fournier-Sicre, F. Fell, and D. Stramski (2003), Light scattering properties of marine particles in coastal and open ocean waters as related to the particle mass concentration, *Limnol. Oceanogr.*, *48*(2), 843–859.

Bader, H. (1970), The hyperbolic distribution of particle sizes, *J. Geophys. Res.*, *75*(15), 2822–2830.

Bass, M., E. W. Van Stryland, D. R. Williams, and W. L. Wolfe (Eds.) (1995), *Handbook of Optics–Volume I Fundamentals, Techniques, and Design*, 2nd ed., 43.21 pp., McGraw-Hill, New York.

Bergmann, T., G. Fahnenstiel, S. Lohrenz, D. Millie, and O. Schofield (2004), Impacts of a recurrent resuspension event and variable phytoplankton community composition on remote sensing reflectance, *J. Geophys. Res.*, *109*, C10S15, doi:10.1029/2002JC001575.

Berk, A., G. P. Anderson, P. K. Acharya, M. L. Hoke, J. H. Chetwynd, L. S. Bernstein, E. P. Shettle, M. W. Matthew, and S. M. Adler-Golden (2003), *MODTRAN4 Version 3 Revision 1 User's Manual*, Air Force Research Laboratory, Hanscom AFB, MA.

Bohren, C., and D. R. Huffman (1983), *Absorption and Scattering of Light by Small Particles*, Wiley, New York.

Bowers, D. G., and C. E. Binding (2006), The optical properties of mineral suspended particles: A review and synthesis, *Estuarine, Coastal Shelf Sci.*, *67*, 219–230.

Brando, V. E., and A. G. Dekker (2003), Satellite hyperspectral remote sensing for estimating estuarine and coastal water quality, *IEEE Trans. Geosci. Remote Sens.*, *41*(6), 1378–1387.

Bricaud, A., and A. Morel (1986), Light attenuation and scattering by photoplanktonic cells: A theoretical modeling, *Appl. Opt.*, *25*, 571–580.

Bukata, R. P., J. H. Jerome, K. Y. Kondratyev, and D. V. Pozdnyakov (1995), *Optical Properties and Remote Sensing of Inland Coastal Waters*, 362 pp., CRC, Boca Raton, FL.

Chander, G., B. L. Markham, and J. Barsi (2007), Revised Landsat 5 thematic mapper radiometric calibration, *IEEE Trans. Geosci. Remote Sens. Lett.*, *4*, 490–494.

Curran, P. J., and E. M. M. Novo (1988), The relationship between suspended sediment concentration and remotely sensed spectral radiance: A review, *J. Coastal Res.*, *4*, 351–368.

Dekker, A. G., R. J. Vos, and S. W. M. Peters (2001), Comparison of remote sensing data, model results and in situ data for total suspended matter (TSM) in the southern Frisian lakes, *Sci. Total Environ.*, *268*, 197–214.

Durand, D., J. Bijaoui, and F. Cauneau (2000), Optical remote sensing of shallow-water environmental parameters: A feasibility study, *Remote Sens. Environ.*, *73*(2), 152–161.

Egan, W. G., and T. W. Hilgeman (1979), *Optical Properties of Inhomogeneous Materials: Applications to Geology, Astronomy, Chemistry, and Engineering*, 235 pp., Academic, New York.

Eshel, G., G. J. Levy, U. Mingelgrin, and M. J. Singer (2004), Critical evaluation of the use of laser diffraction for particle-size distribution analysis, *Soil Sci. Soc. Am. J.*, *68*, 736–743.

Frette, Ø., J. J. Stamnes, and K. Stamnes (1998), Optical remote sensing of marine constituents in coastal waters: A feasibility study, *Appl. Opt.*, *16*(1), 202–204.

Gaudoin, O., B. Yang, and M. Xie (2003), A simple goodness-of-fit test for the power-law process, based on the Duane plot, *IEEE Trans. Reliab.*, *52*(1), 69–74.

Gillespie, J. B., J. D. Lindberg, and M. S. Smith (1974), Visible and near-infrared absorption coefficients of montmorillonite and related clays, *Am. Mineral.*, *59*, 1113–1116.

Gould, R. W., and R. A. Arnone (1997), Estimating the beam attenuation coefficient in coastal waters from AVHRR imagery, *Cont. Shelf Res.*, *17*(11), 1375–1387.

Green, R. E., and H. M. Sosik (2004), Analysis of apparent optical properties and ocean color models using measurements of seawater constituents in New England continental shelf surface waters, *J. Geophys. Res.*, *109*, C03026, doi:10.1029/2003JC001977.

Gregg, W. W., and K. Carder (1990), A simple spectral solar irradiance model for cloudless maritime atmospheres, *Limnol. Oceanogr.*, *35*, 1657–1675.

Harrison, A. W., and C. A. Coombes (1988), An opaque cloud cover model of sky short wavelength radiance, *Solar Energy*, *41*(4), 387–392.

Holyer, R. J. (1978), Toward universal multispectral suspended sediment algorithms, *Remote Sens. Environ.*, *7*, 323–338.

Hoogenboom, H. J., A. G. Dekker, and J. F. de Haan (1998), Retrieval of chlorophyll and suspended matter from imaging spectrometry data by matrix inversion, *Can. J. Remote Sens.*, *24*(2), 144–151.

Jonasz, M., and G. R. Fournier (2007), *Light Scattering by Particles in Water: Theoretical and Experimental Foundations*, Elsevier, London.

Kirk, J. T. O. (1994), *Light and Photosynthesis in Aquatic Ecosystems*, Cambridge University Press, Cambridge.

Legleiter, C. J., D. A. Roberts, A. W. Marcus, and M. A. Fonstad (2004), Passive optical remote sensing of river channel morphology and in-stream habitat: Physical basis and feasibility, *Remote Sens. Environ.*, *93*, 493–510.

Marcus, A. W., and M. A. Fonstad (2010), Remote sensing of rivers: The emergence of a subdiscipline in the river sciences, *Earth Surf. Process. Landforms*, *35*, 1867–1872.

Meade, R. H. (1985), Suspended sediment in the Amazon River and its tributaries in Brazil during 1982–1984. *Open-File Report 85-492*, edited, p. 39, U.S. Geological Survey Open-File Report, Washington, D.C.

Mertes, L. A. K., A. Dekker, G. R. Brakenridge, C. Birkett, and G. Letourneau (2004), *Rivers and Lakes*, edited by S. L. Ustin, pp. 345–400, John Wiley, New York.

Mie, G. (1908), Beiträge zur Optik trüber Medien, speziell kolloidaler Metallösungen, *Ann. Phys.*, *330*(3), 377–445.

Milliman, J. D., and R. H. Meade (1983), World-wide delivery of river sediment to the oceans, *J. Geol.*, *91*(1), 1–21.

Mobley, C. D. (1994), *Light and Water: Radiative Transfer in Natural Waters*, 592 pp., Academic, San Diego, CA.

Mobley, C. D. (1999), Estimation of the remote-sensing reflectance from above-surface measurements, *Appl. Opt.*, *38*, 7442–7455.

Mobley, C. D., and L. K. Sundman (2001), *Hydrolight 4.2 Technical Documentation*, Sequoia Scientific, Redmond, CA.

Munday, J. C., and T. T. Alfoldi (1979), LANDSAT test of diffuse reflectance models for aquatic suspended solids measurement, *Remote Sens. Environ.*, *8*, 169–183.

Ouillon, S., P. Douillet, and S. Andrefouet (2004), Coupling satellite data with in situ measurements and numerical modeling to study fine suspended-sediment transport: A study for the lagoon of New Caledonia, *Coral Reefs*, *23*, 109–122.

Patterson, E. M., D. A. Gillette, and B. H. Stockton (1977), Complex index of refraction between 300 and 700 nm for Saharan aerosols, *J. Geophys. Res. Oceans Atm.*, *82*(21), 3153–3160.

Pavelsky, T. M., and L. C. Smith (2009), Remote sensing of suspended sediment concentration, flow velocity, and lake recharge in the Peace-Athabasca Delta, Canada, *Water Resour. Res.*, *45*, W11417, doi:10.1029/2008WR007424.

Peng, F., S. W. Effler, D. O'Donnell, M. G. Perkins, and A. Weidemann (2007), Role of minerogenic particles in light scattering in lakes and a river in central New York, *Appl. Opt.*, *46*(26), 6577–6596.

Pope, R. M., and E. S. Fry (1997), Absorption spectrum (380–700 nm) of pure water. II. Integrating cavity measurements, *Appl. Opt.*, *36*(33), 8710–8723.

Ritchie, J. C., P. V. Zimba, and J. H. Everitt (2003a), Remote sensing techniques to assess water quality, *Photogram. Eng. Remote Sens.*, *69*(6), 695–704.

Ritchie, J. C., P. V. Zimba, and J. H. Everitt (2003b), Remote sensing techniques to assess water quality, *Photogram. Eng. Remote Sens.*, *69*(6), 695–704.

Roberts, D., K. Halligan, and P. Dennison (2007), *VIPER Tools User Manual*, Univ. of Calif., Santa Barbara, California.

Ruhl, C. A., D. H. Schoellhamer, R. P. Stumpf, and C. L. Lindsay (2001), Combined use of remote sensing and continuous monitoring to analyze the variability of suspended-sediment concentrations in San Francisco Bay, California, *Estuarine, Coastal Shelf Sci.*, *53*, 801–812.

Schiebe, F. R., J. A. Harrington, and J. C. Ritchie (1992), Remote sensing of suspended sediments: The Lake Chicot, Arkansas project, *Int. J. Remote Sens.*, *13*(8), 1487–1509.

Sokolik, I. N., and O. B. Toon (1999), Incorporation of mineralogical composition into models of the radiative properties of mineral aerosol from UV to IR wavelengths, *J. Geophys. Res.*, *104*(D8), 9423–9444.

Stramski, D., M. Babin, and S. B. Wozniak (2007), Variations in the optical properties of terrigenous mineral-rich particulate matter suspended in seawater, *Limnol. Oceanogr.*, *52*(6), 2418–2433.

Stumpf, R. P., and J. R. Pennock (1989), Calibration of a general optical equation for remote sensing of suspended sediments in a moderately turbid estuary, *J. Geophys. Res.*, *94*(C10), 14,363–14,371.

Teillet, P. M., D. L. Helder, B. L. Markham, J. L. Barker, K. J. Thome, R. Morfitt, J. R. Schott, and F. D. Palluconi (2001), A lifetime radiometric calibration record for the Landsat Thematic Mapper, in Proceedings of the Canadian Symposium on Remote Sensing, Quebec City, Quebec.

Toole, D. A., D. A. Siegel, D. W. Menzies, M. J. Neumann, and R. C. Smith (2000), Remote-sensing reflectance determinations in the coastal ocean environment: impact of instrumental characteristics and environmental variability, *Appl. Opt.*, *39*(3), 456–469.

Whitlock, C. H., L. R. Poole, J. W. Usry, W. M. Houghton, W. G. Witte, W. D. Morris, and E. A. Gurganus (1981), Comparison of reflectance with backscatter and absorption parameters for turbid waters, *Appl. Opt.*, *20*(3), 517–522.

Witte, W. G. (1982), Laboratory upwelled radiance and reflectance spectra of Kerr Reservoir sediment waters, *NASA Technical Paper*, 1–19.

Woodruff, D. L., R. P. Stumpf, J. A. Scope, and H. W. Paerl (1999), Remote estimation of water clarity in optically complex estuarine waters, *Remote Sens. Environ.*, *68*, 41–52.

Wozniak, C. B., and D. Stramski (2004), Modeling the optical properties of mineral particles suspended in seawater and their influence on ocean reflectance and chlorophyll estimation from remote sensing algorithms, *Appl. Opt.*, *43*(17), 3489–3503.

N. E. Kilham and D. Roberts, Department of Geography, 1832 Ellison Hall, University of California, Santa Barbara, California, 93106-4060, USA. (nina.kilham@gmail.com)

M. B. Singer, Earth Research Institute, University of California, Santa Barbara, California, 93106-3060, USA.